Cerebral Cortex, 2024, 34, bhae471
https://doi.org/10.1093/cercor/bhae471
Advance access publication date 5 December 2024
Original Article

Testing Hubel and Wiesel's "ice-cube" model of functional maps at cellular resolution in macaque V1

Sheng-Hui Zhang[1,2], Shi-Ming Tang[2,3,4,*], Cong Yu[1,4,*]

[1]School of Psychological aF31Tf0 Tj/F01Tf41Tf7.7(Cgniti)-5.5vre kting Uni-5.5vre[0.1(rsity1278.5,e)]TJ /F3 1 Tf ( )Tj /F4 1 Tf 4[0.15g Y560.3(he)75.6ya RD Cmenere xfor

(Ls)TJ /F3 1 Tf ()Tj ET EMC Link <</MCID1629>>BDC BT 0.0001 Tc /41 1 T

Downloaded from https://academic.oup.com/cercor/article/34/12/bhae471/7917315 by National Science & Technology Library user on 16 December 2024

Received: June 18, 2024. Revised: November 13, 2024. Accepted: November 15, 2024
© The Author(s) 2024. Published by Oxford University Press. All rights reserved. For permissions, please e-mail: journals.permission@oup.com.

Nauhaus et al. 2016) studying

each opposite direction. Recording at a specific viewing distance was completed before moving to the next one, and all stimuli at each relevant distance were pseudo-randomly presented. When a stimulus was presented monocularly to one eye, the other eye was covered with a translucent eye patch, which reduced the impacts of short-term monocular deprivation. During recordings, contralateral and ipsilateral stimulations alternated in blocks of trials, with at least a 10-min break between blocks. During the breaks, the translucent eye mask was off. Each block of trials typically lasted 20 to 25 min.

Two-photon imaging

Two-photon imaging was performed at V1 superficial layers using a Prairie Ultima IV (In Vivo) two-photon microscope (Prairie Technologies) for Monkeys A, C, and D, and a FENTOSmart two-photon microscope (Femtonics) for Monkeys B and E, along with a Ti:sapphire laser (Mai Tai eHP, Spectra Physics). The recording depth was 200 μm for Monkeys A to C, 250 μm for Monkey D, and 210 μm for Monkey E. One FOV measuring 850 × 850 μm^2 was selected in each animal and imaged using a 1,000 nm femtosecond laser under a 16× objective lens (0.8 N.A., Nikon) at a resolution of 1.6 μm/pixel. Fast resonant scanning mode (32 frames per second) was chosen to obtain continuous images of neuronal activity (8 frames per second after averaging every 4 frames). During recording, the strength of fluorescent signals (indicated by the mean luminance of a small area) was monitored and adjusted if necessary to compensate the drift of fluorescent signals.

Imaging data analysis: Initial screening of ROIs

The data were analyzed using customized MATLAB codes. A normalized cross-correlation-based translation algorithm was used to reduce motion artifacts (Li et al. 2017). Then fluorescence changes were associated with corresponding visual stimuli through the time sequence information recorded by the Neural Signal Processor (Cerebus system, Blackrock Microsystem). By subtracting the mean of the four frames before stimuli onset ($F0$) from the average of the sixth–ninth frames after stimuli onset (F) across five or six repeated trials for the same stimulus condition (same orientation, spatial frequency, size, and drifting direction), the differential image ($\Delta F = F - F0$) was obtained.

For a specific FOV, imaging data with ipsilateral and contralateral conditions were combined using a normalized cross-correlation-based translation algorithm on the basis of the same reference images from recordings with the least head movements and highest self-correlations. Then the regions of interest (ROIs) or possible cell bodies were determined through sequential analysis of 432 differential images in the order of spatial frequency (6), size (3), orientation (12), and eye (2) ($6 \times 3 \times 12 \times 2 = 432$). The first differential image was filtered with a band-pass Gaussian filter (size = 2 to 10 pixels), and connected subsets of pixels (>25 pixels, which excluded smaller vertical neuropils) with average pixel value > 3 SD of the mean brightness were selected as ROIs. Then, the areas of these ROIs were set to mean brightness in the next differential image before the bandpass filtering and thresholding were performed. This measure gradually reduced the standard deviations of differential images and facilitated the detection of neurons with relatively low fluorescence responses. If a new ROI and an existing ROI from the previous differential image overlapped, the new ROI would be on its own if the overlapping area (OA) < 1/4 ROI_{new}, discarded if 1/4 ROI_{new} < OA < 3/4 ROI_{new}, and merged with the existing ROI if OA > 3/4 ROI_{new}. The merges would help smooth the contours of the final ROIs. This process was repeated for all 432 differential images twice to select ROIs. Finally, the roundness for each ROI was calculated as:

$$Roundness = \frac{\sqrt{4\pi \times A}}{P}$$

where A was the ROI's area and P was the perimeter. Only ROIs with roundness larger than 0.9, which would exclude horizontal neuropils, were selected for further analysis. The sizes of the ROIs ranged from 3.3 to 19.3 μm in diameter, with an average of 8.9 ± 1.3 μm.

Imaging data analysis: orientation tuning, SF tuning, and ocular dominance

The ratio of fluorescence change ($\Delta F/F0$) was calculated as a neuron's response to a specific stimulus condition. For a specific neuron's response to a specific stimulus condition, the $F0_n$ of the n-th trial was the average of 4 frames before stimulus onset (−500 to 0 ms), and F_n was the average of the fifth to eighth frames after stimulus onset (500 to 1,000 ms). $F0_n$ was then averaged across 12 trials to obtain the baseline $F0$ for all 12 trials (to reduce noises in the calculations of responses), and $\Delta F_n/F0 = (F_n - F0)/F0$ was taken as the neuron's response to this stimulus at the n-th trial. For a small portion of neurons (e.g. 2.1% to 9.8% in Monkeys A to E) showing direction selectivity, as their responses to two opposite directions differed significantly ($P < 0.05$, Friedman test), the six trials at the preferred direction were considered for calculations of $\Delta F_n/F0$ as the neuron's responses to a particular stimulus. $F0$ was still averaged over 12 trials at two opposite directions.

Several steps were then taken to determine whether a neuron was tuned to orientation and/or spatial frequency, and, if so, its ocular dominance index was calculated. For each monocular condition, the orientation, SF, and size (σ) that produced the maximal response among all conditions were selected. Then, responses to the other 11 orientations and 5 SFs were determined at the selected SF and size. Second, to identify orientation and/or SF-tuned neurons, a nonparametric Friedman test was performed to determine whether a neuron's responses at 12 orientations or 6 SFs were significantly different from each other under at least one monocular stimulation. To reduce Type-I errors, the significance level was set at $\alpha = 0.01$. Third, for those showing significant orientation differences, the trial-based orientation responses of each neuron were fitted with a Gaussian model:

$$R(\theta) = a_1 2^{-\left(\frac{\theta - \theta_0}{\sigma}\right)^2} + b$$

where $R(\theta)$ was the response at orientation θ, and the free parameters a_1, θ_0, σ, and b were the amplitude, peak orientation, standard deviation of the Gaussian function, and minimal response of the neuron, respectively. Only neurons with a goodness of fit $R^2 > 0.5$, at least under one monocular stimulation, were finally selected as orientation-tuned neurons (Fig. 1B). The tuned orientation of the neuron was one of two monocular peak orientations that generated a higher response. The amplitude parameter a_1 was positive in all selected orientation neurons. Fourth, for those showing a significant SF difference, the trial-based SF responses of each neuron were further fitted with a difference-of-Gaussian model.

$$R(sf) = a_1 e^{-\left(\frac{sf}{\sigma_1}\right)^2} - a_2 e^{-\left(\frac{sf}{\sigma_2}\right)^2} + b$$

where $R(sf)$ was a neuron's response at spatial frequency sf, the free parameters a_1, σ_1, a_2, and σ_2 were amplitudes and standard

Downloaded from https://academic.oup.com/cercor/article/34/12/bhae471/7917315 by National Science & Technology Library user on 16 December 2024

A

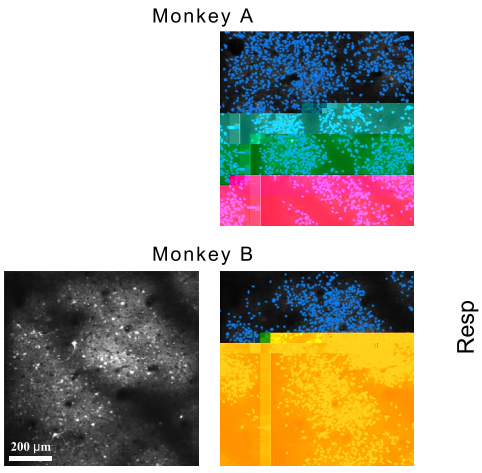

Downloaded from https://academic.oup.com/cercor/article/34/12/bhae471/7917315 by National Science & Technology Library user on 16 December 2024

the intersection angle of one neuron/pixel equals $\left|\frac{1}{2}Angle\left(\vec{R}\right)\right|$, yielding a value between 0° and 90° when $Angle\left(\vec{R}\right)$ is defined within the range of −180° to +180°. Finally, the overall SF-OD intersection angle was determined by the vector sum: $\vec{RO} = \sum_k \vec{R}_k$. The overall SF-OD intersection angle equals $\left|\frac{1}{2}Angle\left(\vec{RO}\right)\right|$, ranges from 0° to 90°. The intersection and overall intersection angle between orientation and SF, along with orientation and OD, were computed in the same manner.

Results

We imaged the responses of V1 superficial-layer neurons to a monocularly (both contralaterally and ipsilaterally) presented Gabor stimulus at various orientations and spatial frequencies in five response FOVs, each from one awake, fixating macaque. The recording depth varied from 200 to 250 μm among FOVs. Each FOV had a size of 850 × 850 μm^2 and was located 1.1° to 3.5° from the central fixation point. Image processing and data analysis identified a total of 9,967 ROIs or possible neurons (Fig. 1A). Among them, 91.2% were tuned to orientation and/or spatial frequency with contralateral and/or ipsilateral stimulus presentations (Friedman test), as exemplified by six neurons in Fig. 1B and C. The ODI of each neuron was calculated as $ODI = (R_i - R_c)/(R_i + R_c)$, where R_i and R_c were the neuron's respective peak responses to ipsilateral and contralateral stimulations. ODI = −1 and 1 would indicate complete contralateral and ipsilateral eye preferences, respectively, and ODI = 0 would indicate equal preferences for both eyes.

Consistent with our earlier report (Ju et al. 2021), the cellular orientation maps displayed significant orientation clustering (Fig. 2A). The cluster indices of the five FOVs ranged from 2.50 to 5.87 (see Materials and Methods for the calculation of cluster indices), with a median cluster index of 3.75 (Fig. 2D). The OD maps (Fig. 2B) also showed clustered neurons, with OD cluster indices ranging from 1.32 to 2.24 and a median of 1.72 (Fig. 2E). The SF maps (Fig. 2C) displayed a limited range of SF tuning, with few neurons tuned to low SFs. Furthermore, SF clustering was weak, with cluster indices ranging from 1.06 to 1.67 and a median of 1.37 (Fig. 2F; a clustering index of 1 indicates zero clustering). These SF results replicate our previous data collected from different macaques with the same procedure (Guan et al. 2021) and are consistent with earlier single-unit results showing an approximately two-octave SF tuning range in V1 neurons (De Valois et al. 1982) and weak or insignificant SF clustering (Edwards et al. 1995; DeAngelis et al. 1999).

To determine the geometric relationships among orientation, OD, and SF maps, we first calculated the respective orientation, OD, and SF gradients for each target neuron in three types of functional maps (Fig. 3A–C). Specifically, we located all neurons within a radius of 400 μm from a target neuron and defined vectors with the target neuron as the coinitial point and these nearby neurons as terminal points. For each pair of target and nearby neurons, the orientation/OD/SF vector magnitudes were the differences of their preferred orientations/ODs/SFs, respectively. We then summed the orientation/OD/SF vectors of all neuron pairs, respectively, with each vector normalized by the distance between the neuron pair, as the target neuron's orientation/OD/SF gradient (see Materials and Methods). The outcomes of gradient computation were largely stable and robust to changes for radii than 150 μm (Fig. 3D).

It is evident that, within the same subarea of a specific FOV, there are often clustered gradient lines along one direction in one gradient map and an orthogonal direction in a different gradient map (e.g. the white-circled region in Ori and OD maps of Monkey A, Fig. 3), or along similar directions in a pair of gradient maps (e.g. the yellow-circled region in Ori and OD maps of Monkey A, Fig. 3). As a result, functional maps exhibit coexisting orthogonal and parallel relationships, as well as other pairings of intersection angles, which are quantified below.

The intersection angles among the orientation, OD, and SF gradients of each neuron were determined by the differences among the directions of these gradients. When necessary, the intersection angles were transformed to be within the range of 0° to 90° (see Materials and Methods, Fig. 4A–C). It is evident that there were no consistent concentrations of intersection angles between ORI and OD maps and between ORI and SF maps (Fig. 4D). Specifically, the intersection angles on average (weighted means) were flat (ORI-OD) or nearly flat with a few % difference between 0° and 90° intersections (ORI-SF) (Fig. 4D). The intersections between SF-OD maps appeared to be parallel more frequently, which was mainly contributed by two FOVs (with 10% more neurons having 0° intersections than 90° intersections), while the other three FOVs showed flatter functions. Additional contour plots were also presented in Supplemental Fig. S1, in which additional data points were added to cellular functional maps using a natural neighbor interpolation method before each map was convolved by a 2D Gaussian ($\sigma = 25$ μm). These plots reveal no significant trends for orthogonal or parallel intersections either.

Together, these cellular maps failed to display a structure in which the OD-ORI and ORI-SF relationships were predominantly orthogonal and the SF-OD relationship was predominantly parallel, as predicted by previous pixel-based functional maps. Furthermore, the intersection angles are clustered (Fig. 4E). This clustering was determined by the gradient maps. For example, when the orientation and OD gradients of neurons in a subarea of an FOV were respectively similar—often caused by similar orientation and OD preferences of these neurons, or by orientation and OD preferences varying at a similar rate—the intersection angles of orientation and OD maps in the same subarea were also similar and clustered.

We refined the analysis in several ways to examine the above outcomes. First, to remove potential measurement errors and cell variances, we divided the 512 pixel × 512 pixel images into grids, each of which was 8 × 8, 16 × 16, or 32 × 32 pixels in size, and averaged the selectivity of neurons within each grid. The patterns of intersection angles did not show any consistent patterns, especially no parallel or orthogonal concentrations, as shown in Supplemental Fig. S2, which displays exemplar maps of feature tunings, gradients, and intersection angles with grids of 32 × 32 pixels. Second, because of the small image size and the blood vessel occlusion, the calculation of the gradient could be inaccurate for neurons close to the edge of the image or to the vessels. We reperformed the calculations after removing these neurons and found basically unchanged results (Supplemental Fig. S3). Third, previously, Yu et al. (2005) reported that the orthogonal relationships were present at locations where the gradients of both the orientation and ocular dominance maps were within the top 30th percentile. However, this trend was not evident in our data either when only the intersection angles of neurons with top 30 percentile gradient values were considered (

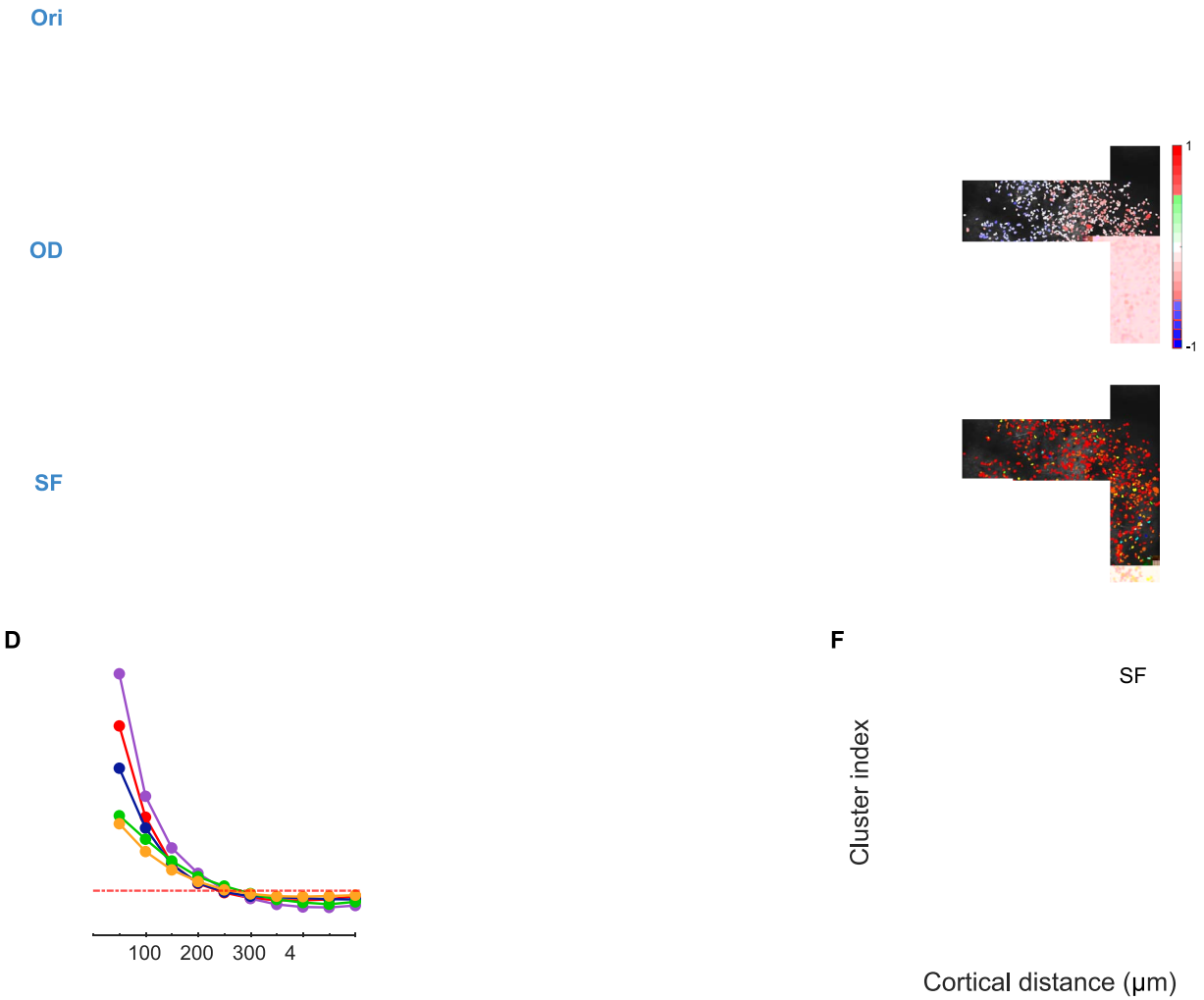

Downloaded from https://academic.oup.com/cercor/article/34/12/bhae471/7917315 by National Science & Technology Library user on 16 December 2024

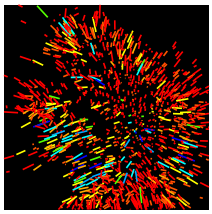

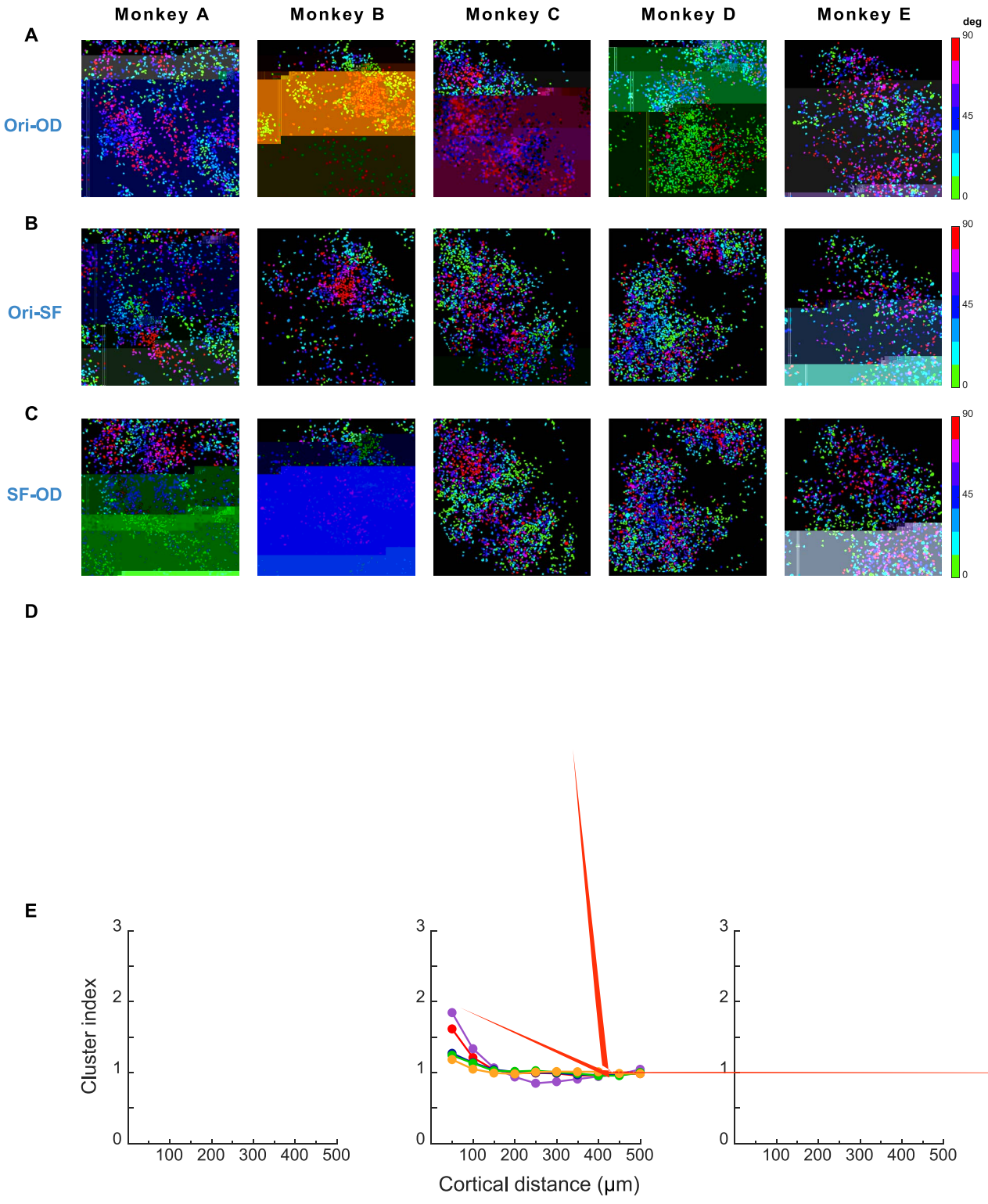

Downloaded from https://academic.oup.com/cercor/article/34/12/bhae471/7917315 by National Science & Technology Library user on 16 December 2024

Downloaded from https://academic.oup.com/cercor/article/34/12/bhae471/7917315 by National Science & Technology Library user on 16 December 2024

Intersection an

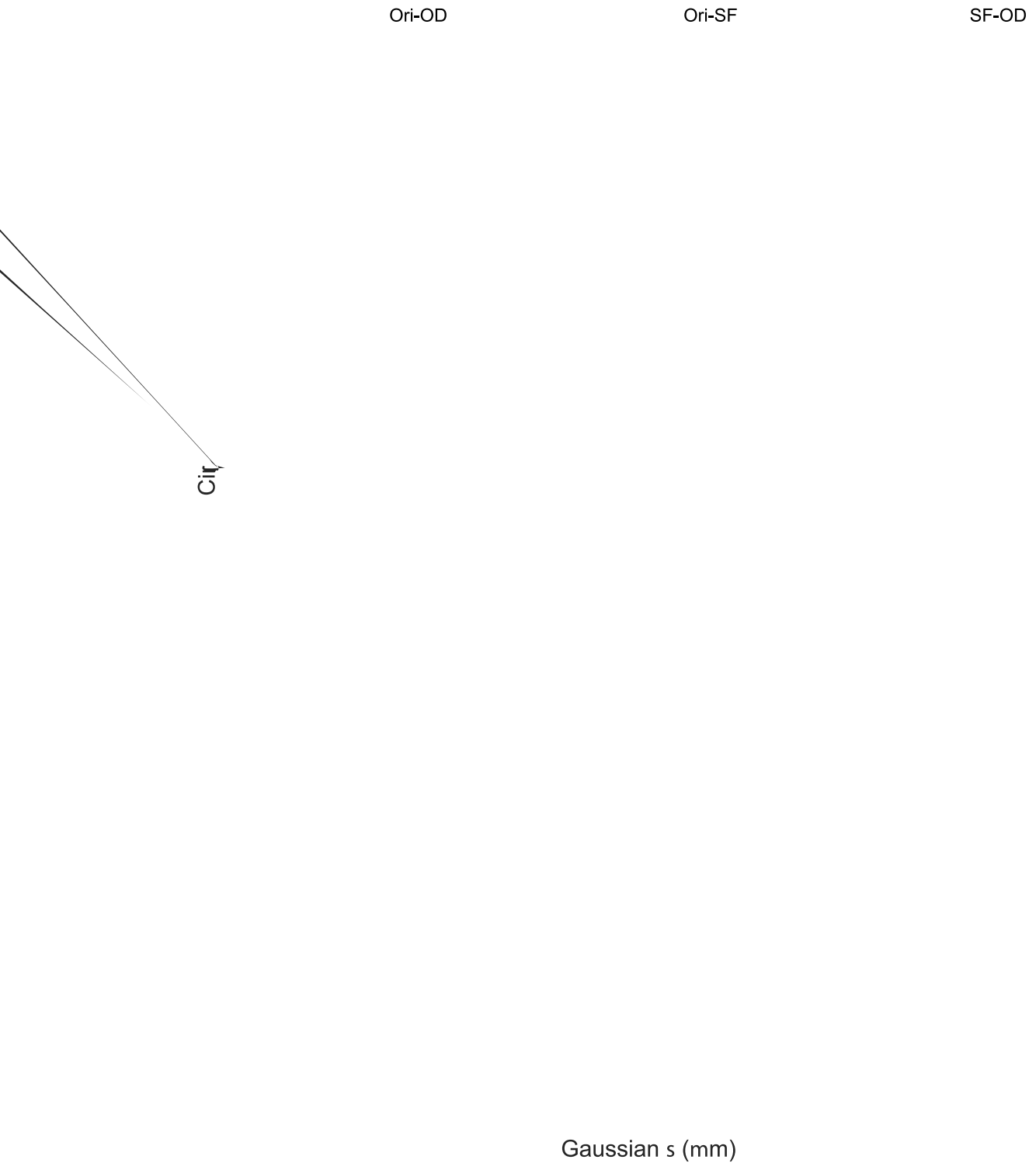

Downloaded from https://academic.oup.com/cercor/article/34/12/bhae471/7917315 by National Science & Technology Library user on 16 December 2024

Author contributions

Sheng-Hui Zhang (Data curation, Formal analysis, Writing—original draft), Shi-Ming Tang (Methodology, Writing—review & editing), and Cong Yu (Conceptualization, Formal analysis, Writing—review & editing).

Supplementary material

Supplementary material is available at *Cerebral Cortex* online.

Funding

This study was supported by a STI2030-Major Projects grant (2022ZD0204600), Natural Science Foundation of China grants (31230030 and 31730109), and funds from Peking-Tsinghua Center for Life Sciences, Peking University.

Conflict of interest statement: None declared.

References

Bartfeld E, Grinvald A. Relationships between orientation-preference pinwheels, cytochrome oxidase blobs, and ocular-dominance columns in primate striate cortex. *Proc Natl Acad Sci USA*. 1992:89:11905–11909. https://doi.org/10.1073/pnas.89.24.11905.

Basole A, White LE, Fitzpatrick D. Mapping multiple features in the population response of visual cortex. *Nature*. 2003:423:986–990. https://doi.org/10.1038/nature01721.

Das A, Gilbert CD. Long-range